JCTC Journal of Chemical Theory and Computation

pubs.acs.org/JCTC Article

Coupling Monte Carlo, Variational Implicit Solvation, and Binary Level-Set for Simulations of Biomolecular Binding

Zirui Zhang,‖ Clarisse G. Ricci,‖ Chao Fan, Li-Tien Cheng,* Bo Li,* and J. Andrew McCammon

Cite This: J. Chem. Theory Comput. 2021, 17, 2465−2478 Read Online

ACCESS | Metrics & More | Article Recommendations

ABSTRACT: We develop a hybrid approach that combines the Monte Carlo (MC) method, a variational implicit-solvent model (VISM), and a binary level-set method for the simulation of biomolecular binding in an aqueous solvent. The solvation free energy for the biomolecular complex is estimated by minimizing the VISM free-energy functional of all possible solute−solvent interfaces that are used as dielectric boundaries. This functional consists of the solute volumetric, solute−solvent interfacial, solute−solvent van der Waals interaction, and electrostatic free energy. A technique of shifting the dielectric boundary is used to accurately predict the electrostatic part of the solvation free energy. Minimizing such a functional in each MC move is made possible by our new and fast binary level-set method. This method is based on the approximation of surface area by the convolution of an indicator function with a compactly supported kernel and is implemented by simple flips of numerical grid cells locally around the solute−solvent interface. We apply our approach to the p53-MDM2 system for which the two molecules are approximated by rigid bodies. Our efficient approach captures some of the poses before the final bound state. All-atom molecular dynamics simulations with most of such poses quickly reach the final bound state. Our work is a new step toward realistic simulations of biomolecular interactions. With further improvement of coarse graining and MC sampling, and combined with other models, our hybrid approach can be used to study the free-energy landscape and kinetic pathways of ligand binding to proteins.

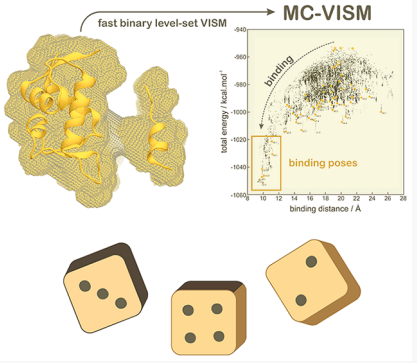

I. INTRODUCTION

Biomolecular binding in aqueous solvent is fundamental to biological functions yet extremely complex due to the many-body interactions spanning across multiple temporal and spatial scales. Recent years have seen a growing interest in understanding the mechanisms of such biomolecular processes, due to particularly the rapid development in rational drug design.[1−6] However, there are several bottleneck issues in the current computational study of biomolecular binding and unbinding. One of them is the efficient description of the effect of water in the hydration of biomolecules. Water is recognized as an important player in many biomolecular activities, including protein conformational changes, protein−ligand binding and unbinding, and protein−protein interactions.[7−12] This role often results from the collective behaviors of the network of many water molecules. It can therefore be costly to describe the effect of water by including many individual water molecules in computer simulations. Another one is the general issue of crossing free-energy barriers in the binding process in which solute and solvent fluctuations are critical. In general, the process of biomolecular binding can be dominated by either "conformational selection", or "induced fit", or a mix of these.[13−19] Regardless, before reaching a "binding ready" pose, a biomolecular complex is in a diffusional mode, often taking much of the time of the entire binding process.[20]

In this work, we develop a hybrid computational approach to the simulation of biomolecular binding and unbinding processes. This approach combines the Monte Carlo (MC) method, a variational implicit-solvent model (VISM),[21,22] and a new and fast binary level-set method. The MC method is used here to simulate the diffusion of individual proteins and formation of the biomolecular complex, while the VISM with implementation by the binary level-set method is for the efficient estimation of the solvation free energy with an implicit solvent through the solute−solvent interfaces. If we consider two biomolecules immersed in an aqueous solvent, then the free energy for these two molecules to bind or unbind consists of contributions arising from the solute−solute interactions and the solvation of these molecules. Our MC-VISM simulation consists of a sequence of MC moves each of which can be accepted or rejected by the Metropolis criterion with respect to the total interaction free energy.

Received: October 21, 2020
Published: March 2, 2021

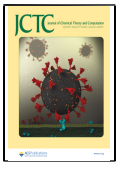

https://dx.doi.org/10.1021/acs.jctc.0c01109
J. Chem. Theory Comput. 2021, 17, 2465−2478

Central in VISM is an effective VISM solvation free-energy functional of all possible solute−solvent interfaces that are used as dielectric boundaries. This functional consists of the solute volumetric, solute−solvent interfacial, solute−solvent van der Waals (vdW) interaction, and electrostatic free energy. For a fixed conformation of the biomolecules, which means particularly that all the solute atoms and their partial charges are fixed, we obtain an estimate of the solvation free energy by numerically minimizing the VISM free-energy functional. In recent years, we have developed the level-set numerical method for such minimization in three-dimensional space with complex protein geometries. Our series of works have demonstrated that the level-set VISM can capture well the solvation free energies, particularly for nonpolar systems, the effect of electrostatics such as the net electrostatic force acting on biomolecules and the subtle step-by-step hydration for charged systems, and the dry and wet hydration states.[23−33] Recently, the efficiency of the VISM is further improved by the coarse-graining through the Martini force field.[34] Moreover, combined with the string method and Brownian dynamics (BD) simulations with a multistate potential, the level-set VISM is also applied to predicting the pathways of dry−wet transitions as well as the kinetics of the molecular binding and unbinding for a model system.[35]

Electrostatics is one of the dominant components of the solvation of charged molecules in an aqueous solvent. In VISM, the electrostatic part of the solvation free energy can be incorporated through the dielectric-boundary Poisson−Boltzmann (PB) theory.[36−41] Here, however, we use the Coulomb-field approximation (CFA), as it requires no solution to partial differential equations and hence is rather efficient.[27,28,30,42] We also use a technique of shifting the dielectric boundary to predict more accurately the electrostatic part of the solvation free energy.[31]

The key to our MC-VISM simulations is our new and fast, binary level-set method for minimizing the VISM free energy done in each of the Metropolis MC moves. This method is based on the approximation of surface area by the convolution of an indicator function with a compactly supported kernel. Instead of a continuous level-set function, here a binary level-set function defined on numerical grid cells is used to define the solute−solvent interface or equivalently the solute and solvent regions. With such a binary level-set function, the VISM free-energy functional can be approximated by summing over the contributions from all the grid cells. We can find a minimum conformation (i.e., the optimal dielectric boundary) of the free-energy functional by iteratively flipping the signature (i.e., the value of the binary level-set function) of the grid cell in a steepest-descent fashion. This formulation does not require solving a partial differential equation. Moreover, the flipping is only done locally around the boundary. Therefore, the method is very fast compared with the classical, continuous level-set method. It is fast enough to be coupled with the MC method for biomolecular simulations. We shall test the convergence, accuracy, and speed of our numerical algorithm by considering single ions in solvent for which analytical and experimental results are available.

We apply our approach to the p53-MDM2 system. The p53-MDM2 interaction is a relevant pharmacological target for anticancer therapeutics[43−47] and an important model for the study of protein−protein binding due to the abundance of structural information.[48−53] MDM2 has a highly concave and hydrophobic binding pocket that undergoes dewetting fluctuations prior to the binding of p53, as seen in our previous explicit solvent molecular dynamics (MD) simulations and level-set VISM calculations.[28,30,54] As capturing different dry and wet states is a characteristic feature of VISM, the choice of p53-MDM2 gives us the chance to compare the performance of the new method to that of the previous version of VISM and to showcase its unique ability to describe desolvation effects. Here, we first calculate the solvation free energy of this protein complex and obtain the potential of mean force with respect to some separation distance of the two molecules. We then approximate each of them as a rigid body and carry out the MC-VISM simulations of their binding process. We show that our efficient approach can capture some of the poses before the final bound state. All-atom MD simulations starting with such poses quickly reach the final bound state.

We now compare briefly our hybrid model with some other implicit-solvent models. In a commonly used, surface based, implicit-solvent model, a solute−solvent interface or dielectric boundary is defined to be a vdW, solvent-excluded, or solvent-accessible surface.[55−59] The solvation free energy is then calculated as the sum of the surface energy, proportional to the area of the surface, and the electrostatic free energy with the PB theory[36−41] or the generalized Born model,[42,60,61] using the surface as a dielectric boundary. Such a fixed-surface model is more efficient than our VISM but requires the adjustment of many parameters. Different dry and wet solvation states are difficult to describe by such a model but are relatively easy to describe by VISM. Both BD simulations[62−65] and our MC-VISM simulations treat the solvent implicitly and use the continuum electrostatics. However, the macroscopic solvent properties used in the two approaches are not all the same. For instance, the bulk solvent density and the solute−solvent interfacial surface tension are the key solvent parameters in our model, while the diffusion tensor is key in BD simulations. Our rigid-body MC-VISM simulations are free-energy based and are designed to sample the distribution of binding poses, while BD simulations are force-based and are often used for the real-time diffusional process and binding rates. One advantage of our approach is its ability of capturing the dry−wet transitions in hydrophobic interactions for macromolecules with complex geometries.

The rest of the paper is organized as follows: In section II, we describe our MC-VISM theory. In particular, we review the VISM free-energy functional with the CFA of the electrostatic solvation free energy. In section III, we describe the binary level-set method for minimizing the VISM free-energy functional and report the results of testing the binary level-set VISM for the solvation of ions. In section IV, we apply our binary level-set VISM to the solvation of the p53-MDM2 complex and show the result of rigid-body MC-VISM simulations of the binding of p53-MDM2. Finally, in section V, we draw our conclusions.

II. THEORY

II.A. The Total Interaction Free Energy. We consider two molecules A (with M atoms) and B (with N atoms) in an aqueous solvent. We denote by $\mathbf{r}_i^A$, Q_i^A ($i = 1, ..., M$) and $\mathbf{r}_j^B$, Q_j^B ($j = 1, ..., N$) all the solute atomic positions and partial charges of A and B, respectively. The total interaction free energy of this molecular complex in the solvent is

$$G_{\text{total}} = G_{\text{vdW,sol−sol}} + G_{\text{elec,sol−sol}} + G_{\text{solvation}} \quad (1)$$

https://dx.doi.org/10.1021/acs.jctc.0c01109
J. Chem. Theory Comput. 2021, 17, 2465−2478

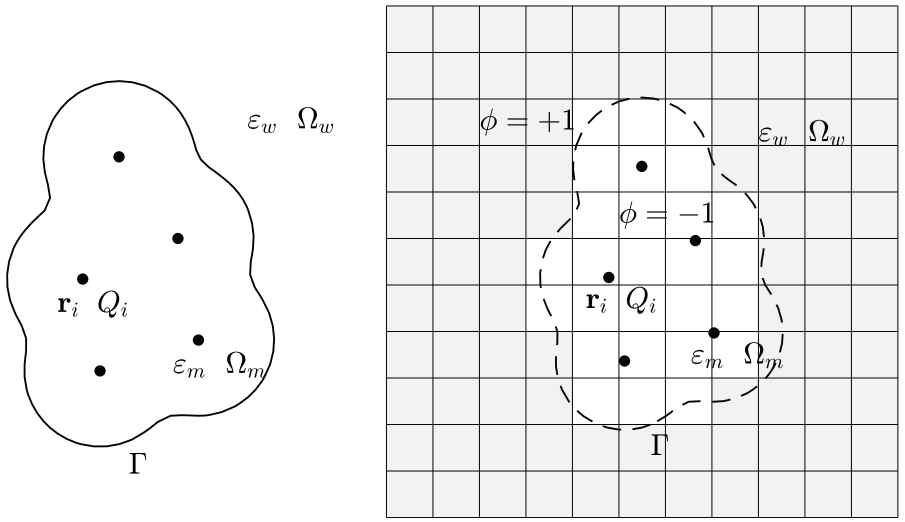

Figure 1. Left: Schematic view of a solvation system with an implicit solvent. A solute−solvent interface Γ separates the solvent region Ω_w from the solute region Ω_m. The solute atoms are located at $\mathbf{r}_1$, ..., $\mathbf{r}_L$ and carry partial charges Q_1, ..., Q_L, respectively. The dielectric permittivities of the solute and solvent regions are denoted by ε_m and ε_w, respectively. Right: In the binary level-set formulation, the computational domain is discretized into grid cells. A binary level-set function is used to approximate the dielectric boundary Γ. It takes the value −1 on any grid cell inside the solute region Ω_m and +1 on any cell inside the solvent region Ω_w; cf. Section III.A.

The first two terms are the solute−solute van der Waals (vdW) and electrostatic interaction energies, given by the Lennard-Jones (LJ) and Coulomb interaction potentials, respectively

$$G_{\mathrm{vdW,sol-sol}} = \sum_{i=1}^{M}\sum_{j=1}^{N} 4\varepsilon_{ij}\left[\left(\frac{\sigma_{ij}}{|\mathbf{r}_i^A - \mathbf{r}_j^B|}\right)^{12} - \left(\frac{\sigma_{ij}}{|\mathbf{r}_i^A - \mathbf{r}_j^B|}\right)^{6}\right]$$

$$G_{\mathrm{elec,sol-sol}} = \frac{1}{4\pi\varepsilon_0\varepsilon_w}\sum_{i=1}^{M}\sum_{j=1}^{N}\frac{Q_i^A Q_j^B}{|\mathbf{r}_i^A - \mathbf{r}_j^B|}$$

Here, ε_{ij} and σ_{ij} are the energy and length parameters of the LJ potential for the interaction between $\mathbf{r}_i^A$ and $\mathbf{r}_j^B$, ε_0 is the vacuum permittivity, and ε_w is the relative permittivity of the solvent. The solvation free energy $G_{\mathrm{solvation}}$ is given by

$$G_{\mathrm{solvation}} = \min_{\Gamma} G_{\mathrm{VISM}}[\Gamma]$$

Here, $G_{\mathrm{VISM}}[\Gamma]$ is the VISM solvation free energy of a solute−solvent interface Γ that encloses all the solute atoms, and the minimum is taken over all such interfaces Γ. This functional $G_{\mathrm{VISM}}[\Gamma]$ is described in more details for a general setup in the next subsection.

II.B. The VISM Free-Energy Functional. Consider one or more molecules of solute atoms located at $\mathbf{r}_i$ and carrying partial charges Q_i (i = 1, ..., L) (In the case of two molecules as described above, the total number of solute atoms is $L = M + N$.). For any closed surface Γ that encloses all the solute atoms $\mathbf{r}_i$, we denote by Ω_m and Ω_w the interior and exterior of the surface Γ and call them the solute and solvent regions, respectively; cf. Figure 1 (Left). We also call Γ a solute−solvent interface. We shall denote by ε_m the dielectric permittivity of the solute region Ω_m.

The VISM solvation free-energy functional of all possible solute−solvent interfaces Γ is defined by[21,22,31,33]

$$G_{\mathrm{VISM}}[\Gamma] = \Delta P\mathrm{vol}(\Omega_m) + \int_\Gamma \gamma dS + \rho_w \sum_{i=1}^{L}\int_{\Omega_w} U_i(|\mathbf{r} - \mathbf{r}_i|)dV_{\mathbf{r}} + G_{\mathrm{elec}}[\Gamma] \quad (2)$$

Here, the first term $\Delta P\mathrm{vol}(\Omega_m)$ describes the energy of creating the solute region Ω_m in the solvent, where ΔP is the difference of the pressure of the solvent liquid and solute vapor, respectively. In this work, we shall neglect this term as it is rather small compared with other terms.[22]

The second term is the surface energy, where γ is the solute−solvent interfacial surface tension. In general, we can take the form $\gamma = \gamma_0(1-2\tau H)$, where γ_0 is the constant surface tension for a planar liquid−vapor interface, τ is the curvature correction coefficient known as the Tolman length,[66,67] and H is the local mean curvature (the average of the two principal curvatures) that is positive for a spherical solute. While the Tolman correction is often found to be useful in many cases,[23,26,27,31,33] it can also be more complicated and costly in computations. Therefore, as the coupling of our VISM with MC simulatons requires rather efficient implementation, in this work, we shall neglect this correction.

The third term is the solute−solvent vdW type interaction energy. The constant ρ_w is the bulk solvent number density. For each i, the term $U_i(|\mathbf{r}-\mathbf{r}_i|)$ is the vdW type interaction potential between the solute atom at $\mathbf{r}_i$ and a solvent molecule or ion at $\mathbf{r}$. We employ the LJ potential

$$U_i(r) = 4\varepsilon_i\left[\left(\frac{\sigma_i}{r}\right)^{12} - \left(\frac{\sigma_i}{r}\right)^{6}\right] \quad (3)$$

where the parameters ε_i of energy and σ_i of length can vary with solute atoms as in a conventional force field.

The last term $G_{\mathrm{elec}}[\Gamma]$ in eq 2 is the electrostatic part of the solvation free energy. Here we shall use the Coulomb-field approximation (CFA):[27,28,30,42]

https://dx.doi.org/10.1021/acs.jctc.0c01109
J. Chem. Theory Comput. 2021, 17, 2465−2478

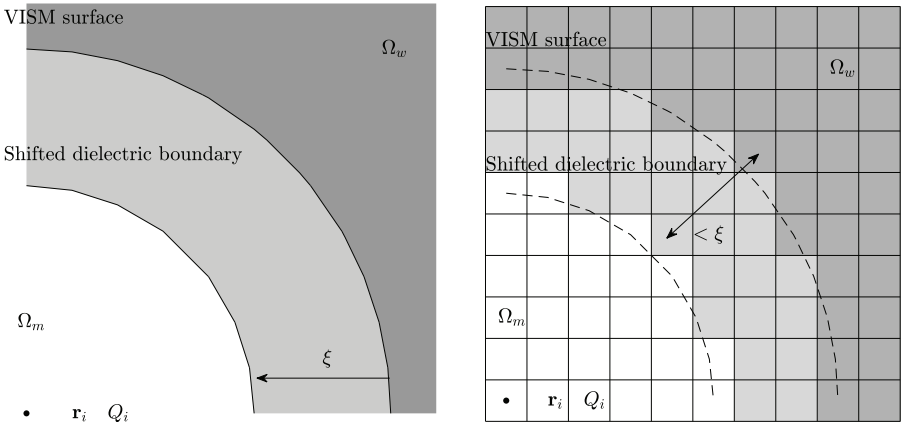

Figure 2. Left: An effective dielectric boundary is obtained by shifting the VISM surface inward to the solute region by ξ (Å). Right: In the binary level-set implementation, a grid cell in the solute region Ω_m contributes to the electrostatic energy, if it has a center-to-center distance less than ξ to some grid cell in the solvent region Ω_w.

$$G_{\text{elec}}[\Gamma] = \frac{1}{32\pi^2\varepsilon_0}\left(\frac{1}{\varepsilon_w} - \frac{1}{\varepsilon_m}\right)\int_{\mathbb{R}^3\setminus\Omega_m}\left|\sum_{i=1}^{L}\frac{Q_i(\mathbf{r}-\mathbf{r}_i)}{|\mathbf{r}-\mathbf{r}_i|^3}\right|^2 dV_{\mathbf{r}} \quad (4)$$

Note that the integral is over the entire region outside the solute region Ω_m. This accounts for the long-range effect of the Coulomb interaction.

For a given set of solute atomic positions $\mathbf{r}_i$ and partial charges Q_i (i = 1, ..., L), we can now minimize the VISM solvation free-energy functional $G_{\text{VISM}}[\Gamma]$ to obtain an optimal solute−solvent interface. It has been found that such a VISM surface, i.e., a VISM free-energy minimizing surface, often represents the surface with the first peak of water density determined using the position of oxygen atoms in water molecules[27,28,30,31] and may not be necessarily the best choice of dielectric boundary. In fact, if we use a VISM surface as the dielectric boundary to calculate the electrostatic solvation energy, then the error can be sometimes significant.[27,28,30,31] Here we use a previously developed technique to shift the VISM surface by a constant distance ξ (usually ξ = 1 Å) toward the solute region; cf. Figure 2 (Left). The shifted boundary is an effective dielectric boundary and is used to the final calculation of the electrostatic free energy.

II.C. The MC-VISM Algorithm and Parameters. We now consider the binding of two molecules A and B as described in Section II.A. The solute atomic positions and the corresponding partial charges are $\mathbf{r}_i^A$, Q_i^A (i = 1, ..., M) and $\mathbf{r}_j^B$, Q_j^B (j = 1, ..., N), respectively. The total binding free energy of such a molecular complex is given in eq 1. To explore the complex binding process, we approximate the two molecules as rigid bodies. This means that the position of the molecules A and B is determined by their centers of mass $\mathbf{R}^A$ and $\mathbf{R}^B$ and the orientation of the smaller molecule relative to the larger one. We also fix the larger molecule throughout the simulation.

The MC-VISM Algorithm for the Binding of Two Molecules.

Step 1. Initialize the system: set up the initial atomic positions of the molecules and input all the parameters.

Step 2. Randomly perturb the smaller molecule. Perturbations include both rigid-body rotations and translations.

Step 3. Calculate the solute−solute vdW and Coulomb interaction energies.

Step 4. Calculate the solvation free energy by minimizing the VISM free-energy functional.

Step 5. Calculate the total binding free energy $G_{\text{total}}^{\text{new}}$ and the free-energy difference $\Delta G = G_{\text{total}}^{\text{new}} - G_{\text{total}}^{\text{old}}$.

Step 6. If $\Delta G < 0$, then accept the MC move. Otherwise, generate a random number $\alpha \in [0,1]$ and accept the move if and only if $e^{-\Delta G/k_BT} \le \alpha$.

Step 7. If a predefined total number of MC moves is reached, then stop. Otherwise, go to Step 2.

We use the LJ parameters from the force field in CHARMM36.[68,69] In Table 1, we list the VISM parameters.

Table 1. VISM Parameters

parameter	symbol	value	unit
temperature	T	298	K
solvent number density	ρ_w	0.0333	Å^{-3}
surface tension	γ_0	0.174	k_BT/Å^2
solute dielectric constant	ε_m	1	
solvent dielectric constant	ε_w	80	
boundary shift	ξ	1	Å

III. NUMERICAL METHOD

III.A. A Binary Level-Set Method. We describe in detail our new, binary level-set method for numerically minimizing the VISM free-energy functional eq 2 (with $\Delta P = 0$ and $\tau = 0$). We choose a computational box $\Omega = (-A,A)^3$ that contains completely the entire solute region Ω_m, where $2A$ (in Å) is the side length. Note that the solvation region Ω_w can be larger than Ω. We cover the computational box Ω with a uniform finite difference grid with grid size (i.e., the side of each grid cell) h. We define a binary level-set function ϕ on Ω with such a grid by $\phi(\mathbf{x}) = 1$ or -1 on each grid cell.[70] With such a binary level-set function, we obtain the (approximate) solute region Ω_m and solvent region Ω_w to be the union of all the grid cells with ϕ-value -1 and that with 1, respectively; cf. Figure 1 (Right). We shall consider only those binary level-set functions with the corresponding solute region Ω_m containing all the solute atoms $\mathbf{r}_1$, ..., $\mathbf{r}_L$. The solute−solvent interface Γ is still defined to be the interface that separates the solute and solvent regions, but it is now composed of a collection of faces of grid cells.

With a binary level-set formulation, we can discretize the VISM free-energy functional eq 2 (with $\Delta P = 0$ and $\tau = 0$). Since the solvent region Ω_w is larger than the computational

https://dx.doi.org/10.1021/acs.jctc.0c01109
J. Chem. Theory Comput. 2021, 17, 2465−2478

box Ω, the region of integral Ω_w of the vdW interaction term, the third term in eq 2 which is now denoted as $G_{vdW}[\Gamma]$, is divided into two parts: one part within the computational box $\Omega_w \cap \Omega$ and the remaining part $\Omega_w \backslash \Omega$. Similarly, the integral region $\mathbb{R}^3 \backslash \Omega_m$ in eq 4, the Coulomb-field approximation of the electrostatic energy, is divided into two parts: $\Omega_w \cap \Omega$ and $\mathbb{R}^3 \backslash \Omega$ By using the center-point integration rule, we obtain

$$G_{vdW}[\Gamma] = \sum_{\mathbf{x}_j \in \Omega_w \cap \Omega} (G_{vdW})_j + G_{vdW}(\Omega_w \backslash \Omega) + O(h) \tag{5}$$

$$G_{elec}[\Gamma] = \sum_{\mathbf{x}_j \in \Omega_w \cap \Omega} (G_{elec})_j + G_{elec}(\mathbb{R}^3 \backslash \Omega) + O(h) \tag{6}$$

where $\mathbf{x}_j$ is the center of the jth grid cell in the solvent region $\Omega_w \subseteq \Omega$, and the notation $O(h)$ indicates that the discretization error is of the order of h. For each j

$$(G_{vdW})_j = \rho_w \sum_{i=1}^{L} U_i(|\mathbf{x}_j - \mathbf{r}_i|) h^3 \tag{7}$$

$$(G_{elec})_j = \frac{1}{32\pi^2 \varepsilon_0} \left(\frac{1}{\varepsilon_w} - \frac{1}{\varepsilon_m} \right) \left| \sum_{i=1}^{L} \frac{Q_i(\mathbf{x}_j - \mathbf{r}_i)}{|\mathbf{x}_j - \mathbf{r}_i|^3} \right|^2 h^3 \tag{8}$$

The term $G_{vdW}(\Omega_w \backslash \Omega)$ in eq 5 and the term $G_{elec}(\mathbb{R}^3 \backslash \Omega)$ in eq 6 are the corresponding integrals over $\Omega_w \backslash \Omega$ and $\mathbb{R}^3 \backslash \Omega$, respectively. They both can be approximated by integrals of the form

$$\int_{B(\mathbf{0},\hat{A}) \backslash B(\mathbf{0},A)} I_{\Omega \backslash B(\mathbf{0},A)} f(x, y, z) dV$$

where $B(\mathbf{0},a)$ denotes the ball centered at the origin $\mathbf{0}$ with radius a, $\hat{A}$ is a cutoff number, $I_{\Omega \backslash B(\mathbf{0},A)}$ is the indicator function of $\Omega \backslash B(\mathbf{0},A)$ (i.e., it takes the value 1 on $\Omega \backslash B(\mathbf{0},A)$ but 0 elsewhere), and $f(x,y,z)$ represents the corresponding integrand. This integral can then be written analytically as iterated integrals using the spherical coordinates and evaluated by one-dimensional numerical quadrature (e.g., the midpoint rule). For the case of the vdW interaction, the cutoff $\hat{A}$ can be chosen not so large so that the calculation of $G_{vdW}(\Omega_w \backslash \Omega)$ is fast. For the case of the electrostatic energy, we can choose $\hat{A} = \infty$ (i.e., no cutoff) and then change the variable $r \to 1/r$ for the one-variable integral over $r \in (A,\infty)$. The calculation then turns out to be very fast.

We remark that if a large number of solute atoms are fixed in simulation, then we could compute all the corresponding contributions $(G_{vdw})_j$ and $(G_{elec})_j$ before any interaction loop and store these values for use throughout the entire simulation.

With $\tau = 0$ in eq 2, the surface energy is $\gamma_0 \text{Area}(\Gamma)$. To approximate the surface area using a binary level-set function ϕ, we introduce a kernel function $K = K(\mathbf{x})$ ($\mathbf{x} \in \mathbb{R}^3$). We assume that the kernel is non-negative and radially symmetric (i.e., $K(\mathbf{x})$ is a one-variable function of $|\mathbf{x}|$) and that the kernel vanishes outside the unit ball $B_1(\mathbf{0})$ (the ball centered at the origin with radius 1) of the three-dimensional space $\mathbb{R}^3$; cf. Figure 3. We approximate the surface area of Γ by

$$\text{Area}(\Gamma) = C(\delta) \int_{\mathbf{x} \in \Omega_m} \int_{\mathbf{y} \in \Omega_w} K\left(\frac{\mathbf{x} - \mathbf{y}}{\delta} \right) d\mathbf{y} d\mathbf{x} + O(\delta^2)$$
$$\text{for } 0 < \delta \ll 1 \tag{9}$$

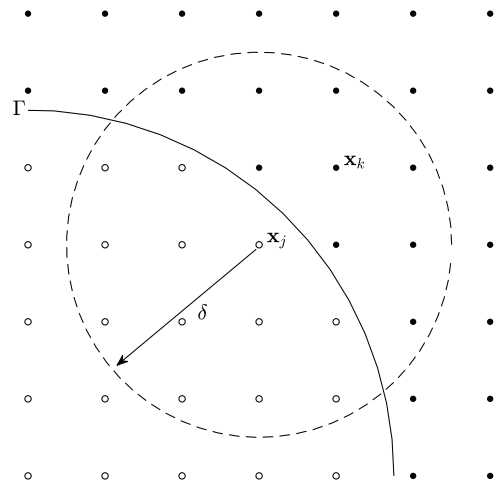

Figure 3. Illustration of a scaled kernel centered at the center $\mathbf{x}_i$ of a grid cell and vanishing outside a sphere (indicated by the broken lines). Black dots represent centers of grid cells in the solvent region Ω_w, and circles represent the centers of grid cells in the solute region Ω_m.

where

$$C(\delta) = \left(\delta^4 \int_0^1 a_0(s) ds \right)^{-1} \quad \text{and} \quad a_0(s) = \int_{B_1(\mathbf{0}) \cap \{y_3 > s\}} K(\mathbf{y}) d\mathbf{y}$$

In the integral region for the definition of $a_0(s)$, y_3 is the third component of the position vector $\mathbf{y}$. A similar formula can be found in the literature on diffusion generated motion by mean curvature,[71−76] where the area is approximated by convolution with the Gaussian kernel. The idea here is that the surface area of the interface between two regions is related to the amount of substance that diffuses from one region to the other. Optimizing the area formula with respect to δ leads to the choice of $\delta \sim \sqrt{h}$. The discretization of the double-integral in eq 9 by the center-point numerical integration rule then leads to

$$\gamma_0 \text{Area}(\Gamma) = \sum_{\mathbf{x}_j \in \Omega_m} (G_{surf})_j + O(h) \tag{10}$$

$$(G_{surf})_j = \gamma_0 C(\delta) h^6 \sum_{\substack{\mathbf{x}_k \in \Omega_w \\ |\mathbf{x}_k - \mathbf{x}_j| \le \delta}} K(\mathbf{x}_j - \mathbf{x}_k) \tag{11}$$

In our implementation of the binary level-set method, we use the kernel function

$$K(\mathbf{x}) = \begin{cases} \sin^2(\pi |\mathbf{x}|) & \text{if } |\mathbf{x}| \le 1 \\ 0 & \text{otherwise} \end{cases}$$

We also choose $\delta = 3\sqrt{h}$. From numerical experimentation, we find this choice of kernel function and rescaled kernel radius δ produces robust results.

It now follows from eqs 5, 6, and 10 that the final, discretized VISM free energy is given by

$$G_{VISM}^{disc} = \sum_{\mathbf{x}_j \in \Omega_m} (G_{surf})_j + \sum_{\mathbf{x}_j \in \Omega_w} [(G_{vdW})_j + (G_{elec})_j] + G_{vdW}(\Omega_w \backslash \Omega) + G_{elec}(\mathbb{R}^3 \backslash \Omega)$$

https://dx.doi.org/10.1021/acs.jctc.0c01109
J. Chem. Theory Comput. 2021, 17, 2465−2478

Note that we can use this formula to calculate the free-energy change if we flip the signature (i.e., the sign) of the binary level-set function at the center $\mathbf{x}_j$ of an arbitrary grid cell. Suppose we change a grid cell centered at $\mathbf{x}_j$ from Ω_m to Ω_w, which corresponds to filling the void by water, then the change in G_{VISM}^{disc} due to the flipping is

$$\Delta G_j = \gamma_0 C(\delta) h^6 \sum_{\substack{\mathbf{x}_k \in \Omega_m \\ |\mathbf{x}_k - \mathbf{x}_j| < \delta}} K(\mathbf{x}_j - \mathbf{x}_k) - \gamma_0 C(\delta) h^6 \sum_{\substack{\mathbf{x}_k \in \Omega_w \\ |\mathbf{x}_k - \mathbf{x}_j| < \delta}} K(\mathbf{x}_j - \mathbf{x}_k) + (G_{vdW})_j + (G_{elec})_j \tag{12}$$

Notice that the first two terms together are the difference between the kernel in the water region and that in the solute region. Similarly, if we change $\mathbf{x}_j$ from Ω_w to Ω_m, which corresponds to removing water from this cell, the resulting energy change is $-\Delta G_j$. We remark that for our algorithm to work we need to assume the surface to be smooth and the grid size to be small so that the radius of the kernel is smaller than the smallest radius of circle of curvature for the interface.

Our binary level-set method for minimizing the VISM free-energy functional is an optimization method of the steepest descent type. Therefore, due to the nonconvexity of the VISM free-energy functional, different initial surfaces may relax to different local minimizers of the free-energy functional that are metastable equilibria. Such local minimizers correspond to polymodal hydration states. In order to capture different local minimizers, we usually use two types of initial surfaces: a tight wrap that is a union of the surfaces of vdW spheres centered at solute atoms with reduced radii and a loose wrap that is a large surface loosely enclosing all the solute atoms; cf. Figure 4.

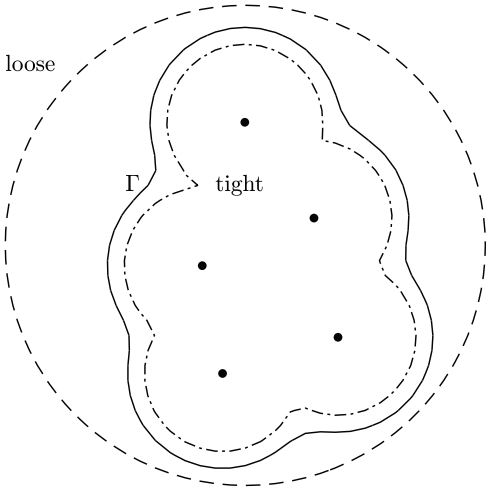

Figure 4. Illustration of a tight initial surface (dot-broken line), a loose initial surface (broken line), and a VISM surface (i.e., a VISM relaxed surface, solid line) Γ surrounding solute atoms (dots).

After a surface is initialized, we can calculate the difference ΔG_j (cf. eq 12) at every center of the grid cell near the interface Γ. The minimization of the total (discrete) free energy G_{VISM}^{disc} is done by repeatedly flipping the grid cell with the most negative ΔG_j, thus leading to a steepest descent in total energy. After each flipping, the value of ΔG_j at neighboring grid cells within the rescaled kernel radius δ needs to be updated. The algorithm stops when $\Delta G_j > 0$ for every grid cell, which means there is no single flipping that could decrease the total energy, and we reach a local minimum. We note that there may be simultaneous flippings at multiple grid cells that can lead to a global minimum. Since we need to repeatedly look up the grid cell with the minimum value of ΔG_j, we can use the min-heap data structure, which takes logarithmic time to remove the smallest element and insert an element.[77]

III.B. Algorithm. Algorithm of the Binary Level-Set Method.

Step 1. Input all the parameters γ_0, ρ_w, ε_0, ε_m, ε_w, and atomic parameters $\mathbf{r}_i$, Q_i, ε_i, and σ_i, for all $i = 1, ..., L$. Choose a computational box according to the atomic coordinates and discretize the box uniformly with the prescribed computational grid size h. Initialize the kernel function and the binary level-set function (tight or loose).

Step 2. Compute and store $(G_{vdW})_j$ (cf. eq 7) and $(G_{elec})_j$ (cf. eq 8) at centers $\mathbf{x}_j$ of all grid cells.

Step 3. Compute $(G_{geom})_j$ (cf. eq 11) and ΔG_j (cf. eq 12) at each center $\mathbf{x}_j$ of the grid cell. Insert the pair $(\mathbf{x}_j, \Delta G_j)$ to the heap data structure.

Step 4. Find the grid cell with minimum ΔG_j, flip its signature, and update ΔG_k at the neighboring center point $\mathbf{x}_k$ with $|\mathbf{x}_j - \mathbf{x}_k| \le \delta$.

Step 5. Repeat Step 4 until $\Delta G_j > 0$ for all grid cells. At this point, we reach a local minimum where there is no single flipping that can decrease the energy.

III.C. Test on Single Ions. To test the VISM and the binary level-set method, we consider an ion or, more generally, a spherical molecule with a single charged atom at its center (assumed to be the origin **0**) carrying a partial charge Q. The VISM free-energy functional eq 2 (with $\Delta P = 0$ and $\tau = 0$) is then a function of the radius R of that spherical solute region. It is given by

$$G(R) = 4\pi R^2 \gamma_0 + 16\pi \rho_w \varepsilon \left(\frac{\sigma^{12}}{9R^9} - \frac{\sigma^6}{3R^3} \right) + \frac{Q^2}{8\pi \varepsilon_0 R} \left(\frac{1}{\varepsilon_w} - \frac{1}{\varepsilon_m} \right) \tag{13}$$

where $\sigma = \sigma_1$ and $\varepsilon = \varepsilon_1$ are the LJ parameters in the LJ potential for the interaction between the charged molecule and a water molecule; cf. eq 2 and eq 3. The function $G(R)$ can be minimized very accurately.

We use the parameters in Table 1 and set $\sigma = 3.5$ Å and $\varepsilon = 0.3 k_B T$. We consider different partial charge values $Q = 0$ e, 0.5 e, and 1 e. For each of these values, we minimize the function $G(R)$ (cf. eq 13) to get the minimum value of the solvation free energy. We also use a continuous level-set method and our new, binary level-set method to minimize the VISM free-energy functional eq 2 with the current parameters and with the computational box $\Omega = (-8,8)^3$ Å^3. In Table 2, we show the results of our computations. The result of the minimization of the function $G(R)$ (cf. eq 13) is labeled "analytic". The result obtained by the continuous level-set method is labeled "continuous", while that by the binary level-set method is labeled "binary". It is clear that our binary level-set VISM is very accurate compared with the continuous level-set VISM for a single charged particle.

We also apply our binary level-set VISM to the solvation of single ions K^+, Na^+, Cl^-, and F^-. We take the LJ parameters for

https://dx.doi.org/10.1021/acs.jctc.0c01109
J. Chem. Theory Comput. 2021, 17, 2465−2478

Table 2. Solvation Free Energy (in k_BT) and Its Components for a Particle with Different Charge Values Q (in e)

	surface energy			vdW energy			electrostatic energy		
Q	analytical	continuous	binary	analytical	continuous	binary	analytical	continuous	binary
0	20.51	20.68	20.28	−2.64	−2.76	−2.66	0.00	0.00	0.00
0.5	19.27	19.43	19.16	−1.05	−1.24	−1.26	−23.17	−23.08	−23.10
1	16.89	17.01	16.72	5.11	4.78	4.89	−99.01	−98.65	−98.87

these ions from the publication.[78] In our calculations, the dielectric boundary of the anion Cl^- or F^- is obtained by shifting the VISM equilibrium surface by ξ = 1 Å, which is the length of the water OH bond.[27,28,79−82] In Table 3, we display the solvation free energy obtained by our continuous and binary level-set VISM calculations and the experimental values of solvation free energy[83] for these ions. We see that our VISM result agrees well with experiment.

Table 3. Solvation Free Energy (in k_BT) for Each of the Single Ions K^+, Na^+, Cl^-, and F^-: The Level-Set VISM Calculations vs Experiment[83]

ions	ε (k_BT)	σ (Å)	experiment	continuous level-set	binary level-set
K^+	0.008	3.85	−117.5	−112.3	−103.1
Na^+	0.008	3.49	−145.4	−131.1	−123.1
Cl^-	0.21	3.78	−135.4	−126.7	−113.4
F^-	0.219	3.3	−185.2	−171.9	−158.7

In Table 4, we show a comparison of the calculation speed between the continuous level-set VISM with CPU and the binary level-set VISM with CPU. All the calculations are performed on a 2017 iMac, with 3.5 *GHz Intel Core i5* CPU. The continuous VISM is accurate but slow, and thus, it becomes impractical if we need to compute the energy many times in the simulation. The binary level-set VISM is efficient, and it also approximates well the continuous level-set VISM.

Table 4. Solvation Free Energy (k_BT) and Computation Time (s) for Different Grid Numbers with Q = 0[a]

	surface energy		vdW energy		time	
grid no.	cont	binary	cont	binary	cont	binary
25^3	21.46	20.64	−2.86	−3.31	1.10	0.01
50^3	20.87	20.45	−2.78	−3.02	11.97	0.10
100^3	20.68	20.28	−2.76	−2.66	186.44	1.15
200^3	20.80	20.37	−2.91	−2.68	5032.03	21.21

[a]Here, cont stands for the continuous level-set method, and binary stands for the binary level-set method.

IV. P53-MDM2: SIMULATION RESULTS AND ANALYSIS

IV.A. Solvation Free Energy of p53-MDM2. To test whether the binary level-set VISM can capture the dewetting effects in protein interfaces, we used it to study the solvation behavior in the binding cavity of MDM2 in response to the approach of the p53 transactivation domain peptide. To investigate the heterogeneous hydration induced by p53 in the MDM2 binding pocket with our approach, we generated an artificial dissociation pathway along the axis formed by the geometrical centers of the two proteins in the bound complex (PDB ID 1YCR). The interprotein distance along this reaction coordinate varied from d = 0 (bound crystallographic complex) to d = 24 Å (unbound), with configurations saved every 1 Å. For each configuration, we calculated binary level-set VISM solvation free energies and solute−solvent interfaces, starting from both loose and tight initial surfaces.

Figure 5 shows the differences of the solvation free energy calculated from tight and loose initial surfaces and the individual components of the solvation free energy along the dissociation coordinate, d. For small (d < 10 Å) or large (d > 14 Å) interdomain distances, calculations starting from tight or loose initials converge to the same solvation free energy, indicating they capture similar solvation states ("dry" for short distances and "wet" for large distances). For intermediate distances (10 < d < 14 Å), "branching" of the solvation free energies along the reaction coordinate reveals the existence of heterogeneous solvation states. While tight initial conditions produce fully solvated states, loose initial conditions produce states where water is completely excluded from the interdomain region, as illustrated in Figure 6(A) for d = 13 Å. These results show that binary level-set VISM preserves a significant feature of the original continuous level-set VISM that is the ability to capture different stable minima in the solvation landscape.

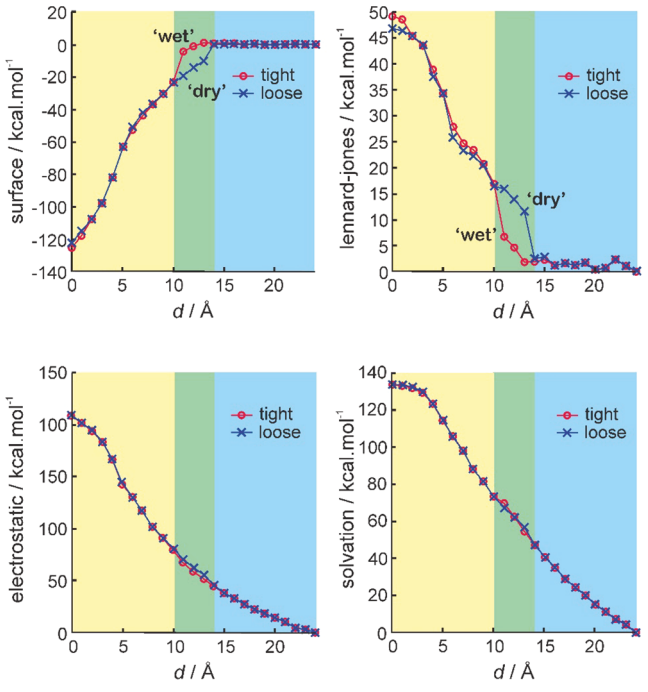

Figure 5. Solvation free energy (and relative components) of MDM2 and p53 along the reaction coordinate, d, obtained from tight and loose initial conditions. Highlighted in yellow and blue are the regions for which loose and tight calculations converge producing either desolvated or solvated states, respectively, and highlighted in green is the region where tight and loose calculations diverge producing different solvation boundaries depending on the initial conditions ("branching").

https://dx.doi.org/10.1021/acs.jctc.0c01109
J. Chem. Theory Comput. 2021, 17, 2465−2478

In the case of MDM2 and p53, the main difference between the dry and wet "branches" consists of the surface component—which favors the "dry branch" by ∼16 kcal/mol—and of the LJ component—which favors the "wet branch" by ∼9 kcal/mol. In terms of the total solvation free energy, however, both "dry" and "wet" branches are similarly stable, indicating that the binding cavity of MDM2 is likely to become desolvated at the approach of p53. The location of the "branching" along the reaction coordinate indicates the critical distance at which wet−dry transitions occur during binding or unbinding. In the case of p53 and MDM2, binary level-set VISM calculations indicate that dewetting transitions occur at 10−14 Å, in relatively good agreement with previous continuous level-set VISM calculations, in which branching was detected at 7.5−15 Å.[30] Differences between binary and continuous level-set VISM results can be attributed to the "pixelation" of solvation boundaries produced by binary VISM and to the fact that in this work we are not using the Tolman coefficient to adjust the surface tension to the local curvature. Figure 6(A) displays the solvation boundaries obtained by

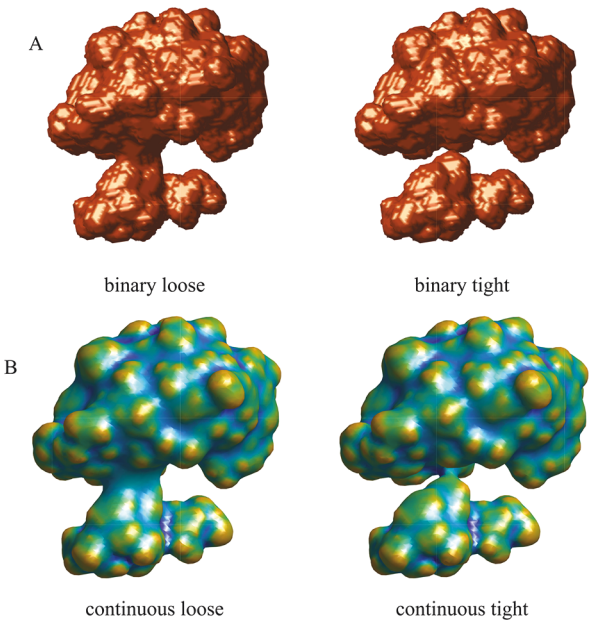

Figure 6. Stable equilibrium solute−solvent interfaces of p53-MDM2 obtained at d = 13 Å by binary (A) or continuous level-set VISM (B), starting from loose (left) or tight (right) initials. In the surfaces produced by the continuous level-set VISM (B), the color of the surface represents the mean local curvature.

binary level-set VISM at d = 13 Å starting from loose or tight initial surfaces. Although pixelated and not including the Tolman correction for local curvature, these solvation boundaries overall capture the same solvation states depicted by continuous level-set VISM at the same separation distance; cf. Figure 6.

We make several remarks on our VISM study of the solvation of p53-MDM2. First, the dry and wet states in the p53-MDM2 complex have been observed in MD simulations and the continuous level-set VISM calculations.[30,54] In particular, from their explicit-solvent MD simulations, Ricci and McCammon[54] observed strong dewetting in the MDM2 binding pocket when the two proteins are apart by <7.6 Å and dewetting fluctuations in the interprotein region when the proteins are apart as far as 15 Å. Second, our binary level-set VISM calculations provided reasonable results on the estimation of free energy and its components, compared with known MD simulations results. For instance, Zhong and Carlson[84] conducted detailed MD simulations and obtained the solute−solute electrostatic interaction energy, solute−solute vdW interaction energy, the solvation electrostatic energy, and the solvation free energy −360.4, −63.8, 369.2, and 359.0 kcal/mol, respectively. We obtained −339.7, −50.5, 385.7, and 313.1 kcal/mol, respectively. Third and finally, with the fast binary level-set method, we obtained each data point in Figure 5 within seconds of computational time.

IV.B. Rigid-Body MC-VISM Simulations of the Binding of p53-MDM2. We then set out to test if the MC-VISM simulations could capture binding events between the p53 peptide and MDM2, starting from random unbound configurations. We start with 10 different initial unbound configurations, marked in Table 5 by s0a and s0b (same conformation) and s1, ..., s9. These configurations are generated by pulling p53 by 15 Å away from MDM2 along the axis connecting their geometric centers in the bound complex and then, except for the first one (marked s0a and s0b in Table 5), randomly rotating p53 by less than 90°. Initial positions with steric clashes are rejected. A similar setup is used by Zhang et al.[85] to investigate different MC methods. For the first initial conformation, we perform 10 trials; see rows s0a and s0b in Table 5. For each of the other initial conformations s1, ..., s9, we perform five trials. Each trial consists of 100,000 MC moves. The direction of translation and the axis of rotation are uniformly distributed on the unit sphere. The magnitude of translation is uniformly distributed between 0 and 1 Å. The magnitude of rotation is uniformly distributed between 0° and 3.72°. As a metric for binding, we used the average of pairwise distances as proposed by Zhou et al. (2017)[53] (cf. also Figure 9(A)) and herein called the binding distance. Due to the way pairwise distances are combined, the binding distance reflects not only the proximity between the two proteins but also the orientation between them—a large binding distance could correspond to an unbound state or to an incorrectly bound state. Table 5 is a summary of the minimum binding distance and minimum total binding free energy of all the trials.

Figure 7(A) and Figure 8 show the distribution of the many MC-VISM trajectories along the conformational binding space, with initial poses marked by asterisks, final poses marked by circles, and intermediate poses colored from blue to yellow. Many simulations resulted in large binding distances with some decrease in the binding energy, suggesting that p53 engaged in some kind of nonspecific interactions with MDM2, as consistent with the typical rugged topology expected for energy landscapes of binding. Some simulations, however, produced binding distances <12 Å that were accompanied by a sharp and favorable decrease in the binding energy, indicating the formation of specific interactions between p53 and MDM2 (highlighted area in Figure 7(A)). These were considered productive simulations, as they resulted in productive (specific) interactions between p53 and MDM2.

A visual inspection of productive MC simulations reveals that they produced essentially the same binding mode, with the N-terminal portion of the p53 peptide well positioned for binding, while the central Y23 and the C-terminal portion are not yet buried within the MDM2 binding cleft (Figure 7(B)). More specifically, Glu17 (p53) is well positioned to engage in

https://dx.doi.org/10.1021/acs.jctc.0c01109
J. Chem. Theory Comput. 2021, 17, 2465−2478

Table 5. Summary of All Simulations: The Minimum Binding Distance (Å) and Minimum Total Binding Free Energy (kcal/mol) for All the Trials[a]

initial	min binding dist					min total binding free energy				
s0a	9.8	18.8	15.9	15.8	18.6	−1047.18	−988.76	−1002.05	−980.55	−981.13
s0b	15.1	18.1	18.8	17.7	19.1	−978.75	−974.63	−974.46	−972.26	−976.81
s1	19.8	17.2	15.9	15.5	15.2	−982.90	−993.36	−1014.14	−991.34	−996.30
s2	11.1	9.5	14.9	9.8	12.8	−1021.23	−1041.45	−1013.12	−1051.32	−1014.25
s3	10.9	15.0	10.1	15.1	14.9	−1030.65	−987.51	−1046.41	−1004.48	−997.68
s4	19.4	19.1	14.1	19.7	16.8	−994.73	−992.93	−1001.94	−1007.26	−995.31
s5	14.2	15.9	17.2	19.3	13.1	−1003.03	−991.89	−995.71	−989.15	−996.28
s6	13.6	12.7	9.4	15.8	18.4	−1001.05	−994.82	−1049.21	−985.41	−989.17
s7	17.3	18.9	17.2	16.5	15.8	−989.93	−1003.54	−992.42	−1005.80	−991.07
s8	19.2	19.2	17.9	19.9	18.7	−980.08	−989.50	−985.27	−983.36	−983.07
s9	19.4	18.7	16.1	13.9	15.0	−999.90	−993.79	−998.63	−1007.38	−994.79

[a]For the initial configuration, 10 trials are performed; cf. the rows s0a and s0b. For each of the other initial configurations, five trials are performed.

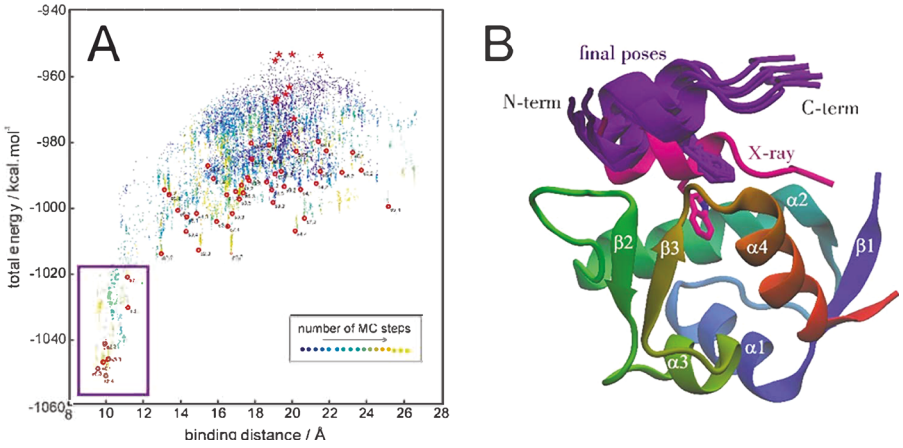

Figure 7. (A) Scatterplot of the total energy as a function of the binding distance for all MC-VISM simulations. Initial (randomly generated) configurations are marked by red asterisks; final configurations are marked by red circles; and configurations sampled throughout the simulations are colored from blue to yellow. MC-VISM simulations resulting in productive binding encounters between p53 and MDM2 are highlighted. For these poses, the RMSD of p53 backbone atoms with respect to the crystal structure (pdb 1cyr) varies from 5.6 to 8.0 Å. (B) Superimposition of the final binding poses from productive MC-VISM simulations (purple) and the X-ray complex (PDB ID 1ycr, in magenta). For reference, the central W23 residue is displayed. The MDM2 secondary structure is colored from the N- to the C-terminal.

electrostatic interactions with Lys94 (MDM2), Thr18 (p53) interacts with Gln72 (MDM2), and Phe19 (p53) is anchored by hydrophobic interactions with Val93 in the binding cleft of MDM2 (not shown). These poses display the characteristics of a prebound state since (i) they display interaction energies that are significantly more favorable than the other final poses, and (ii) they display at least part of the interactions observed in the native bound state (X-ray structure). Our simulations thus suggest that the p53 peptide is initially anchored to MDM2 by its N-terminal end.

Recent experimental and MD simulation studies suggest that p53 binding to MDM2 follows an "induced fly-casting" mechanism, whereby MDM2 initially binds to a partially disordered p53 that only then folds into its final (and more ordered) binding structure.[53] Interestingly, these studies agree that most of the folding occurs in the C-terminal portion and that initial binding occurs with the N-terminal portion of the p53 peptide—in agreement with the prebound state captured by our rigid MC-VISM simulations. The binding mode produced by our MC-VISM simulations captures the same interactions formed in the first half of the "coupled binding-folding" mechanism as proposed by Zhou et al.[53]

It seems reasonable to assume that the main obstacle preventing MC-VISM from reaching the final binding pose is the lack of conformational flexibility, due to steric barriers that cannot be easily overcome with small MC steps. To further investigate this aspect, we used the prebound states produced by MC-VISM as starting points for explicit solvent MD simulations. The final poses from MC-VISM simulations were solvated with TIP3P water molecules,[86] in rectangular boxes of dimensions of 56 × 64 × 66 Å. To each box, Na^+ or Cl^- ions were added to make the systems electrically neutral. Simulations were performed with NAMD 2.12,[87] using the CHARMM36 force field.[68,88] To equilibrate the solvent and the ions, we performed (i) 1000 steps of energy minimization, (ii) 5 ps of NVT simulations at 310 K, and (iii) 500 ps of NPT simulations, at 1 bar and 310 K, to equilibrate the solvent density. All the equilibration stages applied position restraints to the protein atoms. After that, we performed fully flexible simulations for each system at 310 K and 1 bar (NPT regime), for 6 ns.

In six out of the seven MD simulations, p53 quickly tucked the key W23 and C-terminal tail within the MDM2 binding pocket, reaching fully bound states in less than 6 ns of simulations (Figure 9(B),(C)). The final configurations refined by MD simulations were very similar to the crystallographic complex, as shown by the RMSD calculations and visual inspection (Figure 9(D),(E)). In only one simulation, p53

https://dx.doi.org/10.1021/acs.jctc.0c01109
J. Chem. Theory Comput. 2021, 17, 2465−2478

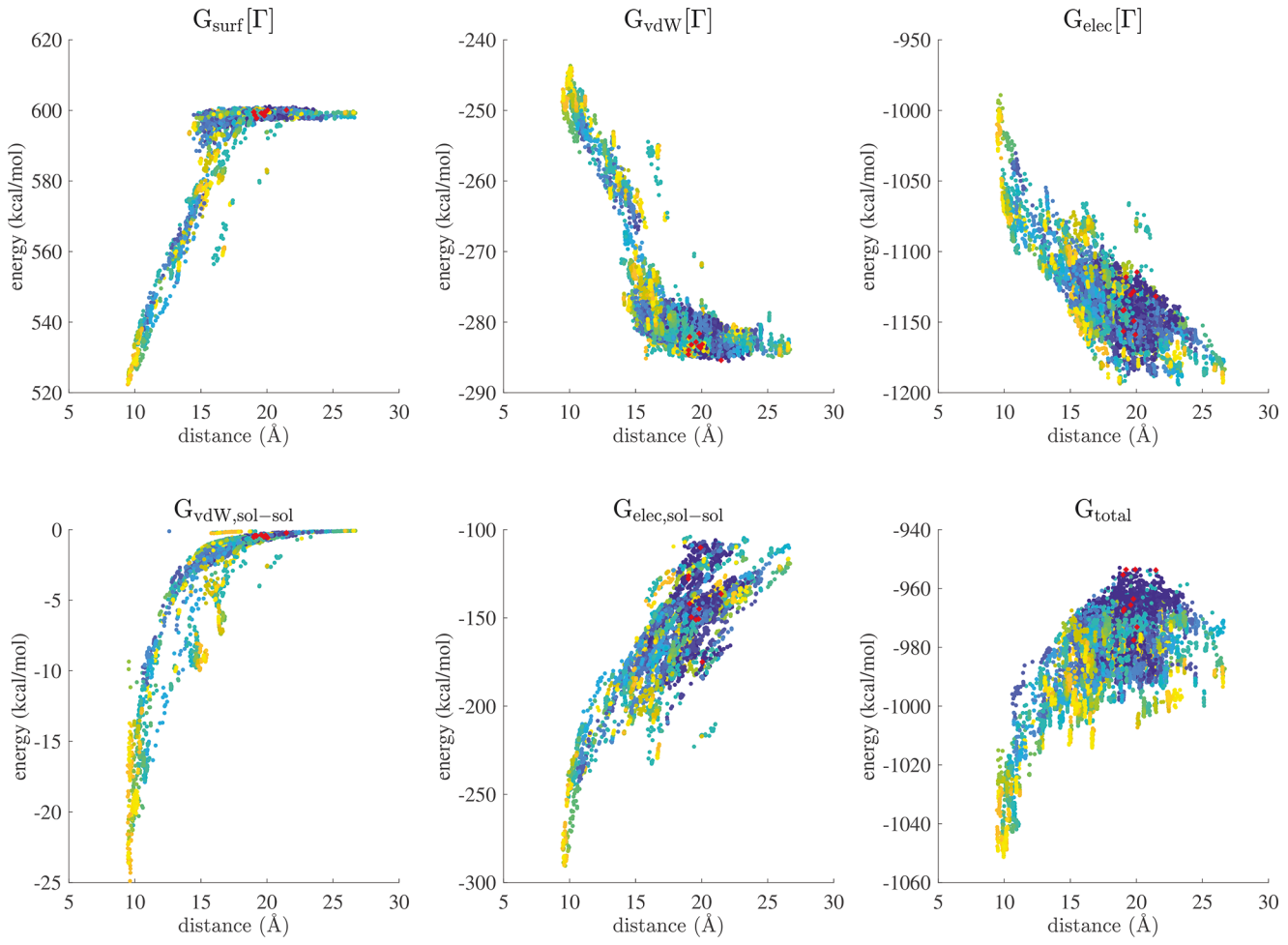

Figure 8. Scatterplot of individual energy components of the total binding energy versus the binding distance for all MC-VISM simulations. Initial (randomly generated) configurations are marked by red circles, and configurations sampled throughout the simulations are colored from blue to yellow.

reached an alternative binding mode in which the side chain of Y19 occupied the central pocket of the MDM2 binding cleft. To conclude, the binding poses predicted by rigid MC-VISM display interactions characteristic of a prebound state and easily lead to the crystallographic binding pose once the proteins are allowed some degree of conformational flexibility.

V. CONCLUSIONS

We have developed a hybrid approach combining the MC method, the VISM for solvation of biomolecules with an implicit solvent, and a fast binary level-set method for the simulation of a biomolecular binding process. We have tested the convergence of our new model and method and applied our approach to the study of protein complex p53-MDM2. We have demonstrated that our binary level-set VISM can efficiently capture heterogeneous hydration states of protein complex p53-MDM2 and that our binary level-set method is fast enough to be coupled with the rigid-body MC simulations of protein−protein interactions. Our extensive rigid-body MC-VISM simulations of binding of p53-MDM2 have captured some initial binding poses of the complex, and MD simulations starting with such poses quickly reach the final bound state. As our final poses capture the same interactions seen in the "bound-before-folded" states as described by Zhou et al.[53] and easily converge into the crystallographic binding pose in short MD simulations, our rigid-body approximations of proteins are a rational and efficient approach to presampling the binding phase space in an approximate manner that can easily be refined by MD simulations.

While our binary level-set method is fast, it is only $O(h)$-accurate with h being the grid size in Å. For our MC-VISM simulations of proteins, we find that there are no visible differences with the choice of h = 0.67 Å and that of h = 0.5 Å, but the results can be different if we use h = 1 Å. In terms of the full MC-VISM simulations, we find that the binding events are less observed if we use h = 1 Å rather than h = 0.67 Å. Therefore, the grid size affects generally the accuracy and speed of our simulations, and we find that the choice of h = 0.5 Å or h = 0.67 Å should be reasonable.

For our VISM relaxation, we have only used a complete tight surface that wraps up all the solute atoms tightly or a complete loose surface that is a large sphere enclosing all the solute atoms. The VISM relaxation of a complete loose surface may capture all the dry spots or pockets on a protein surface. However, in general, there can be many different, partially dry and partially wet, solute−solvent interfaces or protein surfaces. To capture all such surfaces by the VISM relaxation without any fluctuations, we need to construct or sample different, partially tight and partially loose, initial surfaces. When two binding molecules are close enough, there will be only a few

https://dx.doi.org/10.1021/acs.jctc.0c01109
J. Chem. Theory Comput. 2021, 17, 2465−2478

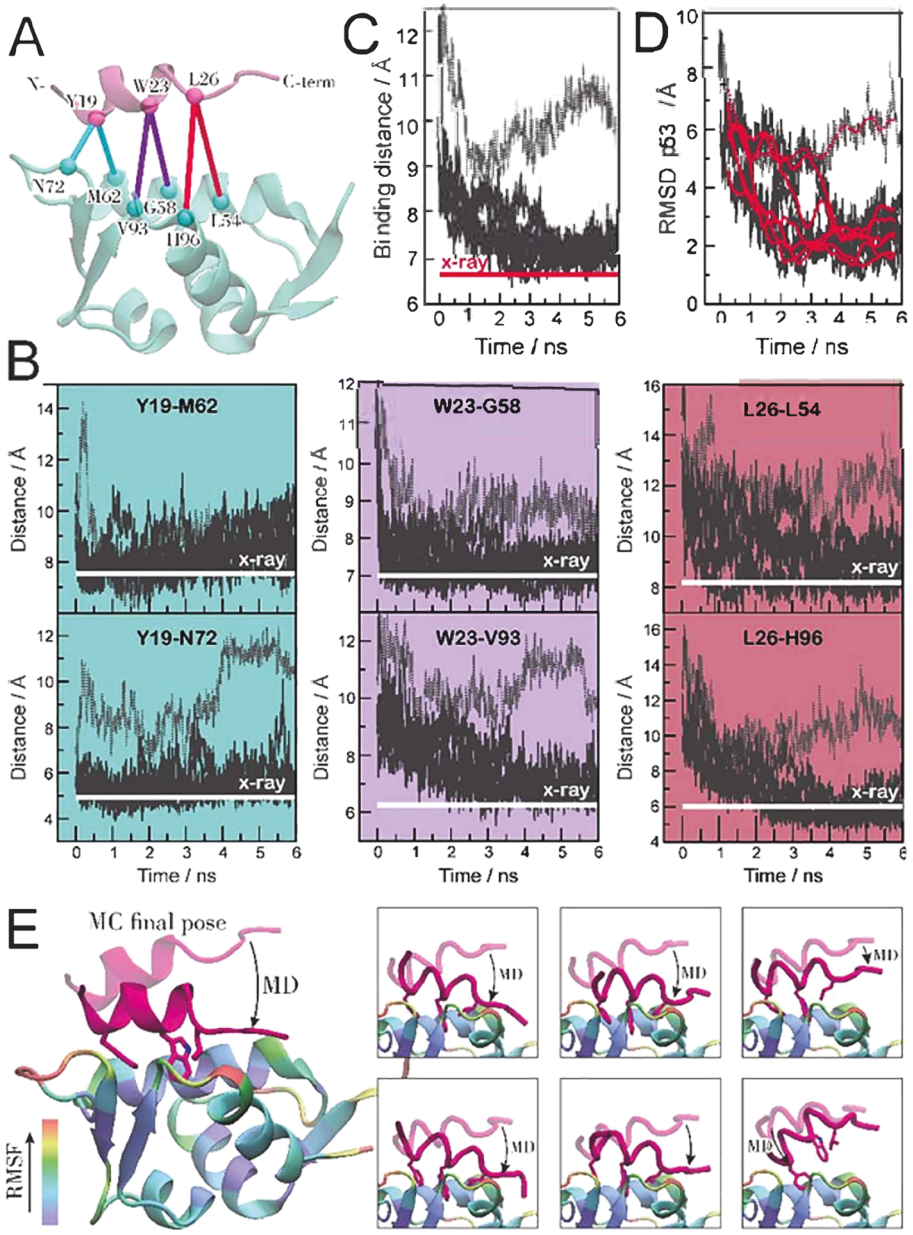

Figure 9. (A) Binding distance as defined by the average of six pairwise distances between p53 and MDM2 α-carbons. (B) Evolution of the pairwise distances involving the N-terminal (cyan panels), the central segment (purple panels), and the C-terminal (red panels) of p53 during the MD simulations. As a reference, the distances as measured in the X-ray complex (PDB ID 1ycr) are shown in white. (C) Evolution of the averaged binding distance during the MD simulations. (D) RMSD of p53 α-carbons with respect to the X-ray structure (PDB ID 1ycr). Alignment was performed based on the α-carbons of MDM2. (E) Refined final poses obtained by MD simulations. For these poses, the RMSD of p53 backbone with respect to the crystal structure (pdb 1cyr) is <2 Å. MDM2 is colored by its backbone RMSF values obtained during the MD simulations. Six out of seven MD simulations rapidly produce the correct binding mode by means of insertion of the C-terminal portion of p53 into the MDM2 binding cleft.

solute atoms around the binding site. For such a case, it is possible to construct different partially tight and partially loose surfaces.

Our future studies shall aim at improving our theory and computations in several aspects. First, we need to include the Tolman correction of the surface energy (cf. eq 2) and the Poisson−Boltzmann equation in our VISM and develop numerical techniques to implement these using our fast binary level-set method. Second, we should address the issue of efficient sampling of all the possible different solvation states that can be captured by setting different initial configurations in the VISM relaxation. Third, we need to relax the restrictions arising from the rigid-body approximations of proteins, as protein flexibility is crucial to the final binding process.[48−50] In this regard, it is possible to develop some coarse-grained models and implementations. Finally, to speed up the MC simulations, we need to accelerate the sampling of binding configurations. An immediate next step can be to implement existing speed-up sampling techniques and combine them into our MC-VISM simulations.

https://dx.doi.org/10.1021/acs.jctc.0c01109
J. Chem. Theory Comput. 2021, 17, 2465−2478

AUTHOR INFORMATION

Corresponding Authors

Li-Tien Cheng − *Department of Mathematics, University of California, San Diego, La Jolla, California 92093-0112, United States*; Email: lcheng@math.ucsd.edu

Bo Li − *Department of Mathematics and Quantitative Biology Ph.D. Program, University of California, San Diego, La Jolla, California 92093-0112, United States*; orcid.org/0000-0002-9183-4654; Email: bli@math.ucsd.edu

Authors

Zirui Zhang − *Department of Mathematics, University of California, San Diego, La Jolla, California 92093-0112, United States*

Clarisse G. Ricci − *Department of Chemistry and Biochemistry, University of California, San Diego, La Jolla, California 92093-0365, United States*; orcid.org/0000-0002-3289-2248

Chao Fan − *Department of Mathematics, University of California, San Diego, La Jolla, California 92093-0112, United States*

J. Andrew McCammon − *Department of Chemistry and Biochemistry, University of California, San Diego, La Jolla, California 92093-0365, United States*; orcid.org/0000-0003-3065-1456

Complete contact information is available at: https://pubs.acs.org/10.1021/acs.jctc.0c01109

Author Contributions

‖Z.Z. and C.G.R. contributed equally.

Notes

The authors declare no competing financial interest.

ACKNOWLEDGMENTS

This work was supported in part by the US National Science Foundation through grant DMS-1913144 (L.-T.C. and B.L.), by the US National Institutes of Health (NIH) through grant R01GM132106 (B.L.), and by a 2019−2020 Lattimer Faculty Research Fellowship, Division of Physical Sciences, University of California, San Diego (B.L.). Work in the McCammon group is supported in part by the NIH (GM31749), the National Biomedical Computation Resource, and the San Diego Supercomputer Center.

REFERENCES

(1) Babine, R. E.; Bender, S. L. Molecular recognition of protein-ligand complexes: Applications to drug design. *Chem. Rev.* **1997**, *97*, 1359−1472.

(2) Morra, G.; Genoni, A.; Neves, M. A.; Merz, K. M. J.; Colombo, G. Molecular recognition and drug-lead identification: What can molecular simulations tell us? *Curr. Med. Chem.* **2010**, *17*, 25−41.

(3) Baron, R.; McCammon, J. A. Molecular recognition and ligand association. *Annu. Rev. Phys. Chem.* **2013**, *64*, 151−175.

(4) Brooijmans, N.; Kuntz, I. D. Molecular recognition and docking algorithms. *Annu. Rev. Biophys. Biomol. Struct.* **2003**, *32*, 335−373.

(5) Michel, J. Current and emerging opportunities for molecular simulations in structure-based drug design. *Phys. Chem. Chem. Phys.* **2014**, *16*, 4465−4477.

(6) Sulimov, V. B.; Kutov, D. C.; Sulimov, A. V. Advances in Docking. *Curr. Med. Chem.* **2020**, *26*, 7555−7580.

(7) Levy, Y.; Onuchic, J. Water mediation in protein folding and molecular recognition. *Annu. Rev. Biophys. Biomol. Struct.* **2006**, *35*, 389−415.

(8) Prabhu, N.; Sharp, K. Protein-solvent interactions. *Chem. Rev.* **2006**, *106*, 1616−1623.

(9) Rasaiah, J. C.; Garde, S.; Hummer, G. Water in nonpolar confinment: From nanotubes to proteins and beyond. *Annu. Rev. Phys. Chem.* **2008**, *59*, 713−740.

(10) Baron, R.; Setny, P.; McCammon, J. A. Water in cavity-ligand recognition. *J. Am. Chem. Soc.* **2010**, *132*, 12091−12097.

(11) Hummer, G. Molecular binding: Under water's influence. *Nat. Chem.* **2010**, *2*, 906−907.

(12) Bellissent-Funel, M.-C.; Hassanali, A.; Havenith, M.; Henchman, R.; Pohl, P.; Sterpone, F.; van der Spoel, D.; Xu, Y.; Garcia, A. E. Water determines the structure and dynamics of proteins. *Chem. Rev.* **2016**, *116*, 7673−7697.

(13) Boehr, D. D.; Wright, P. E. How do proteins interact? *Science* **2008**, *320*, 1429−1430.

(14) Okazaki, K.; Takada, S. Dynamic energy landscape view of coupled binding and protein conformational change: Induced-fit versus population-shift mechanisms. *Proc. Natl. Acad. Sci. U. S. A.* **2008**, *105*, 11182−11187.

(15) Boehr, D. D.; Nussinov, R.; Wright, P. E. The role of dynamic conformational ensembles in biomolecular recognition. *Nat. Chem. Biol.* **2009**, *5*, 789−796.

(16) Hammes, G. G.; Chang, Y.; Oas, T. G. Conformational selection or induced fit: A flux description of reaction mechanism. *Proc. Natl. Acad. Sci. U. S. A.* **2009**, *106*, 13737−13741.

(17) Wlodarski, T.; Zagrovic, B. Conformational selection and induced fit mechanism underlie specificity in noncovalent interactions with ubiquitin. *Proc. Natl. Acad. Sci. U. S. A.* **2009**, *106*, 19346−19351.

(18) Csermely, P.; Palotai, R.; Nussinov, R. Induced fit, conformational selection an independent dynamic segments: An extended view of binding events. *Trends Biochem. Sci.* **2010**, *35*, 539−546.

(19) Zhou, H.-X. From induced fit to conformational selection: A continuum of binding mechanism controlled by the timescale of conformational transitions. *Biophys. J.* **2010**, *98*, L15−L17.

(20) McCammon, J. A. Darwinian biophysics: Electrostatics and evolution in the kinetics of molecular binding. *Proc. Natl. Acad. Sci. U. S. A.* **2009**, *106*, 7683−7684.

(21) Dzubiella, J.; Swanson, J. M. J.; McCammon, J. A. Coupling hydrophobicity, dispersion, and electrostatics in continuum solvent models. *Phys. Rev. Lett.* **2006**, *96*, 087802.

(22) Dzubiella, J.; Swanson, J. M. J.; McCammon, J. A. Coupling nonpolar and polar solvation free energies in implicit solvent models. *J. Chem. Phys.* **2006**, *124*, 084905.

(23) Cheng, L.-T.; Dzubiella, J.; McCammon, J. A.; Li, B. Application of the level-set method to the implicit solvation of nonpolar molecules. *J. Chem. Phys.* **2007**, *127*, 084503.

(24) Cheng, L.-T.; Wang, Z.; Setny, P.; Dzubiella, J.; Li, B.; McCammon, J. A. Interfaces and hydrophobic interactions in receptor-ligand systems: A level-set variational implicit solvent approach. *J. Chem. Phys.* **2009**, *131*, 144102.

(25) Cheng, L.-T.; Xie, Y.; Dzubiella, J.; McCammon, J. A.; Che, J.; Li, B. Coupling the level-set method with molecular mechanics for variational implicit solvation of nonpolar molecules. *J. Chem. Theory Comput.* **2009**, *5*, 257−266.

(26) Setny, P.; Wang, Z.; Cheng, L.-T.; Li, B.; McCammon, J. A.; Dzubiella, J. Dewetting-controlled binding of ligands to hydrophobic pockets. *Phys. Rev. Lett.* **2009**, *103*, 187801.

(27) Wang, Z.; Che, J.; Cheng, L.-T.; Dzubiella, J.; Li, B.; McCammon, J. A. Level-set variational implicit solvation with the Coulomb-field approximation. *J. Chem. Theory Comput.* **2012**, *8*, 386−397.

(28) Guo, Z.; Li, B.; Dzubiella, J.; Cheng, L.-T.; McCammon, J. A.; Che, J. Evaluation of hydration free energy by the level-set variational implicit-solvent model with the Coulomb-Field approximation. *J. Chem. Theory Comput.* **2013**, *9*, 1778−1787.

(29) Zhou, S.; Rogers, K. E.; de Oliveira, C. F.; Baron, R.; Cheng, L.-T.; Dzubiella, J.; Li, B.; McCammon, J. A. Variational implicit-solvent modeling of host-guest binding: A case study on Cucurbit[7]uril. *J. Chem. Theory Comput.* **2013**, *9*, 4195−4204.

(30) Guo, Z.; Li, B.; Dzubiella, J.; Cheng, L.-T.; McCammon, J. A.; Che, J. Heterogeneous hydration of p53/MDM2 complex. *J. Chem. Theory Comput.* **2014**, *10*, 1302−1313.
(31) Zhou, S.; Cheng, L.-T.; Dzubiella, J.; Li, B.; McCammon, J. A. Variational implicit solvation with Poisson-Boltzmann theory. *J. Chem. Theory Comput.* **2014**, *10*, 1454−1467.
(32) Zhou, S.; Sun, H.; Cheng, L.-T.; Dzubiella, J.; Li, B.; McCammon, J. A. Stochastic level-set variational implicit-solvent approach to solute-solvent interfacial fluctuations. *J. Chem. Phys.* **2016**, *145*, 054114.
(33) Ricci, C. G.; Li, B.; Cheng, L.-T.; Dzubiella, J.; McCammon, J. A. Tailoring the variational implicit solvent method for new challenges: Biomolecular recognition and assembly. *Front. Mol. Biosci.* **2018**, *5*, 13.
(34) Ricci, C. G.; Li, B.; Cheng, L.-T.; Dzubiella, J.; McCammon, J. A. Martinizing' the variational implicit solvent method (VISM): Solvation free energy for coarse-grained proteins. *J. Phys. Chem. B* **2017**, *121*, 6538−6548.
(35) Zhou, S.; Weiß, R. G.; Cheng, L.-T.; Dzubiella, J.; McCammon, J. A.; Li, B. Variational implicit-solvent predictions of the dry-wet transition pathways for ligand-receptor binding and unbinding kinetics. *Proc. Natl. Acad. Sci. U. S. A.* **2019**, *116*, 14989−14994.
(36) Davis, M. E.; McCammon, J. A. Electrostatics in biomolecular structure and dynamics. *Chem. Rev.* **1990**, *90*, 509−521.
(37) Sharp, K. A.; Honig, B. Electrostatic interactions in macromolecules: Theory and applications. *Annu. Rev. Biophys. Biophys. Chem.* **1990**, *19*, 301−332.
(38) Baker, N. A. Poisson-Boltzmann methods for biomolecular electrostatics. *Methods Enzymol.* **2004**, *383*, 94−118.
(39) Grochowski, P.; Trylska, J. Continuum Molecular Electrostatics, Salt Effects and Counterion Binding. A Review of the Poisson-Boltzmann Model and its Modifications. *Biopolymers* **2008**, *89*, 93−113.
(40) Che, J.; Dzubiella, J.; Li, B.; McCammon, J. A. Electrostatic free energy and its variations in implicit solvent models. *J. Phys. Chem. B* **2008**, *112*, 3058−3069.
(41) Cai, Q.; Wang, J.; Hsieh, M. J.; Ye, X.; Luo, R. Poisson-Boltzmann implicit solvation models. *Annu. Rep. Comput. Chem.* **2012**, *8*, 149−162.
(42) Bashford, D.; Case, D. A. Generalized Born models of macromolecular solvation effects. *Annu. Rev. Phys. Chem.* **2000**, *51*, 129−152.
(43) Chène, P. Inhibiting the p53-MDM2 interaction: an important target for cancer therapy. *Nat. Rev. Cancer* **2003**, *3*, 102−109.
(44) Khoo, K.; Verma, C.; Lane, D. Drugging the p53 pathway: understanding the route to clinical efficacy. *Nat. Rev. Drug Discovery* **2014**, *13*, 217−236.
(45) Anifowose, A.; Agbowuro, A. A.; Yang, X.; Wang, B. Anticancer strategies by upregulating p53 through inhibition of its ubiquitination by MDM2. *Med. Chem. Res.* **2020**, *29*, 1105−1121.
(46) Duffy, M. J.; Synnott, N. C.; O'Grady, S.; Crown, J. Targeting p53 for the treatment of cancer. *Semin. Cancer Biol.* **2020**, DOI: 10.1016/j.semcancer.2020.07.005.
(47) Jiang, L.; Zawacka-Pankau, J. The p53/MDM2/MDMX-targeted therapies−a clinical synopsis. *Cell Death Dis.* **2020**, *11*, 237.
(48) Uhrinova, S.; Uhrin, D.; Powers, H.; Watt, K.; Zheleva, D.; Fischer, P.; McInnes, C.; Barlow, P. N. Structure of free MDM2 N-terminal domains reveals conformational adjustments that accompany p53-binding. *J. Mol. Biol.* **2005**, *350*, 587−598.
(49) Zondlo, S. C.; Lee, A. E.; Zondlo, N. J. Determinants of specificity of MDM2 for the activation domains of p53 and p65: proline27 disrupts the MDM2-binding motif of p53. *Biochemistry* **2006**, *45*, 11945−11957.
(50) Chen, H. F.; Luo, R. Binding induced folding in p53-MDM2 complex. *J. Am. Chem. Soc.* **2007**, *129*, 2930−2937.
(51) Dastidar, S. G.; Lane, D. P.; Verma, C. S. Multiple peptide conformations give rise to similar binding affinities: molecular simulations of p53-MDM2. *J. Am. Chem. Soc.* **2008**, *130*, 13514−13515.
(52) Borcherds, W.; Theillet, F. X.; Katzer, A.; Finzel, A.; Mishall, K. M.; Powell, A. T.; Wu, H.; Manieri, W.; Dieterich, C.; Selenko, P.; Loewer, A.; Daughdrill, G. W. Disorder and residual helicity alter p53-MDM2 binding affinity and signaling in cells. *Nat. Chem. Biol.* **2014**, *10*, 1000−1002.
(53) Zhou, G.; Pantelopulos, G. A.; Mukherjee, S.; Voelz, V. A. Bridging microscopic and macroscopic mechanisms of p53-MDM2 binding with kinetic network models. *Biophys. J.* **2017**, *113*, 785−793.
(54) Ricci, C. G.; McCammon, J. A. Heterogeneous solvation in distinctive protein-protein interfaces revealed by molecular dynamics simulations. *J. Phys. Chem. B* **2018**, *122*, 11695−11701.
(55) Lee, B.; Richards, F. M. The interpretation of protein structures: Estimation of static accessibility. *J. Mol. Biol.* **1971**, *55*, 379−400.
(56) Richards, F. M. Areas, volumes, packing, and protein structure. *Annu. Rev. Biophys. Bioeng.* **1977**, *6*, 151−176.
(57) Connolly, M. L. Analytical molecular surface calculation. *J. Appl. Crystallogr.* **1983**, *16*, 548−558.
(58) Richmond, T. J. Solvent accessible surface area and excluded volume in proteins. Analytical equations for overlapping spheres and implications for the hydrophobic effect. *J. Mol. Biol.* **1984**, *178*, 63−89.
(59) Connolly, M. L. The molecular surface package. *J. Mol. Graphics* **1993**, *11*, 139−141.
(60) Still, W. C.; Tempczyk, A.; Hawley, R. C.; Hendrickson, T. Semianalytical treatment of solvation for molecular mechanics and dynamics. *J. Am. Chem. Soc.* **1990**, *112*, 6127−6129.
(61) Baker, N. A. Improving implicit solvent simulations: a Poisson-centric view. *Curr. Opin. Struct. Biol.* **2005**, *15*, 137−143.
(62) Ermak, D. L.; McCammon, J. A. Brownian dynamics with hydrodynamic interactions. *J. Chem. Phys.* **1978**, *69*, 1352−1360.
(63) Gabdoulline, R. R.; Wade, R. C. Brownian dynamics simulation of protein-protein diffusional encounter. *Methods* **1998**, *14*, 329−341.
(64) Huber, G. A.; McCammon, J. A. Browndye: a software package for Brownian dynamics. *Comput. Phys. Commun.* **2010**, *181*, 1896−1905.
(65) Huber, G. A.; McCammon, J. A. Brownian dynamics simulations of biological molecules. *Trends Chem.* **2019**, *1*, 727−738.
(66) Tolman, R. C. The effect of droplet size on surface tension. *J. Chem. Phys.* **1949**, *17*, 333−337.
(67) Chen, J.; Brooks, C. L., III Critical importance of length-scale dependence in implicit modeling of hydrophobic interactions. *J. Am. Chem. Soc.* **2007**, *129*, 2444.
(68) Best, R. B.; Zhu, X.; Shim, J.; Lopes, P. E. M.; Mittal, J.; Feig, M.; MacKerell, A. D. Optimization of the additive CHARMM all-atom protein force field targeting improved sampling of the backbone ϕ, ψ and side-chain χ_1 and χ_2 dihedral angles. *J. Chem. Theory Comput.* **2012**, *8*, 3257−3273.
(69) Huang, J.; Rauscher, S.; Nawrocki, G. CHARMM36m: an improved force field for folded and intrinsically disordered proteins. *Nat. Methods* **2017**, *14*, 71−73.
(70) Lie, J.; Lysaker, M.; Tai, X.-C. A binary level set model and some applications to Mumford-Shah image segmentation. *IEEE Trans. Image Proc.* **2006**, *15*, 1171−1181.
(71) Merriman, B.; Bence, J.; Osher, S. Diffusion generated motion by mean curvature. *Computational Crystal Growers Workshop* **1992**, 73−83.
(72) Ruuth, S. J. Efficient algorithms for diffusion-generated motion by mean curvature. *J. Comput. Phys.* **1998**, *144*, 603−625.
(73) Ruuth, S. J.; Merriman, B.; Osher, S. Convolution generated motion as a link between cellular automata and continuum pattern dynamics. *J. Comput. Phys.* **1999**, *151*, 836−861.
(74) Ruuth, S. J.; Merriman, B. Convolution-thresholding methods for interface motion. *J. Comput. Phys.* **2001**, *169*, 678−707.
(75) Esdoğlu, S.; Jacobs, M.; Zhang, P. Kernels with prescribed surface tension and mobility for threshold dynamics schemes. *J. Comput. Phys.* **2017**, *337*, 62−83.

https://dx.doi.org/10.1021/acs.jctc.0c01109
J. Chem. Theory Comput. 2021, 17, 2465−2478

(76) Wang, D.; Li, H.; Wei, X.; Wang, X.-P. An efficient iterative thresholding method for image segmentation. *J. Comput. Phys.* **2017**, *350*, 657−667.
(77) Kleinberg, J.; Tardos, E. *Algorithm Design*; Addison-Wesley Longman Publishing Co., Inc.: USA, 2005.
(78) Horinek, D.; Mamatkulov, S. I.; Netz, R. R. Rational design of ion force fields based on thermodynamic solvation properties. *J. Chem. Phys.* **2009**, *130*, 124507.
(79) Roux, B.; Yu, H. A.; Karplus, M. Molecular basis for the Born mdel of ion solvation. *J. Phys. Chem.* **1990**, *94*, 4683−4688.
(80) Banavali, N. K.; Roux, B. Atomic radii for continuum electrostatics calculation on nucleic acids. *J. Phys. Chem. B* **2002**, *106*, 11026−11035.
(81) Mobley, D. L.; Barber, A. E., II; Fennell, C. J.; Dill, K. A. Charge asymmetries in hydration of polar solutes. *J. Phys. Chem. B* **2008**, *112*, 2405−2414.
(82) Mukhopadhyay, A.; Fenley, A. T.; Tolokh, I. S.; Onufriev, A. V. Charge hydration asymmetry: The basic principle and how to use it to test and improve water models. *J. Phys. Chem. B* **2012**, *116*, 9776−9783.
(83) Marcus, Y. Thermodynamics of solvation of ions. Part 5. Gibbs free energy of hydration at 298.15 K. *J. Chem. Soc., Faraday Trans.* **1991**, *87*, 2995−2999.
(84) Zhong, H.; Carlson, H. A. Computational studies and peptidomimetic design for the human p53-MDM2 complex. *Proteins: Struct., Funct., Genet.* **2005**, *58*, 222−234.
(85) Zhang, Z.; Schindler, C. E. M.; Lange, O. F.; Zacharias, M. Application of enhanced sampling Monte Carlo methods for high-resolution protein-protein docking in Rosetta. *PLoS One* **2015**, *10*, e0125941.
(86) Jorgensen, W. L.; Chandrasekhar, J.; Madura, J. D.; Impey, R. W.; Klein, M. L. Comparison of simple potential functions for simulating liquid water. *J. Chem. Phys.* **1983**, *79*, 926−935.
(87) Phillips, J. C.; Braun, R.; Wang, W.; Gumbart, J.; Tajkhorshid, E.; Villa, E.; Chipot, C.; Skeel, R. D.; Kale, L.; Schulten, K. Scalable molecular dynamics with NAMD. *J. Comput. Chem.* **2005**, *26*, 1781−1802.
(88) Huang, J.; MacKerell, A. D., Jr. CHARMM36 all-atom additive protein force field: Validation based on comparison to NMR data. *J. Comput. Chem.* **2013**, *34*, 2135−2145.

https://dx.doi.org/10.1021/acs.jctc.0c01109
J. Chem. Theory Comput. 2021, 17, 2465−2478